

RHESSI MICROFLARE STATISTICS. II. X-RAY IMAGING, SPECTROSCOPY, AND ENERGY DISTRIBUTIONS

I. G. HANNAH, S. CHRISTE,¹ S. KRUCKER, G. J. HURFORD, H. S. HUDSON, AND R. P. LIN¹

Space Sciences Laboratory, University of California at Berkeley, Berkeley, CA 94720-7450; hannah@ssl.berkeley.edu, schriste@ssl.berkeley.edu, krucker@ssl.berkeley.edu, ghurford@ssl.berkeley.edu, hhudson@ssl.berkeley.edu, rlin@ssl.berkeley.edu

Received 2007 September 19; accepted 2007 December 17

ABSTRACT

We present the first statistical analysis of the thermal and nonthermal X-ray emission of all 25,705 microflares (*RHESSI*) observed between 2002 March and 2007 March. These events were found by searching the 6–12 keV energy range (see Paper I) and are small active region flares, from low (*GOES*) C class to below A class. Each microflare is automatically analyzed at the peak time of the 6–12 keV emission: the thermal source size is found by forward-fitting the complex visibilities for 4–8 keV, and the spectral parameters (temperature, emission measure, power-law index) are found by forward-fitting a thermal plus nonthermal model. The resulting wealth of information we determine about the events allows a range of the thermal and nonthermal properties to be investigated. In particular, we find that there is no correlation between the thermal loop size and the flare magnitude, indicating that microflares are not necessarily spatially small. We present the first thermal energy distribution of *RHESSI* flares and compare it to previous thermal energy distributions of transient events. We also present the first nonthermal power distribution of *RHESSI* flares and find that a few microflares have unexpectedly large nonthermal powers up to 10^{28} erg s⁻¹. The total microflare non-thermal energy, however, is still small compared to that of large flares as it occurs for shorter durations. These large energies and difficulties in analyzing the steep nonthermal spectra suggest that a sharp broken power law and thick-target bremsstrahlung model may not be appropriate for microflares.

Subject headings: Sun: activity — Sun: corona — Sun: flares — Sun: X-rays, gamma rays

Online material: color figures

1. INTRODUCTION

The solar corona exhibits a myriad of transient energy releases over many scales, from large flares down to nanoflares. The frequency distribution of the energy in these events has been studied extensively (Crosby et al. 1993; Shimizu 1995; Krucker & Benz 1998; Aschwanden et al. 2000; Parnell & Jupp 2000; Lin et al. 2001; Aschwanden & Parnell 2002; Benz & Krucker 2002) and has been found to be well represented by a power law of the form

$$dN = AW^{-\alpha} dW, \quad (1)$$

where dN is the number of events per unit time with energy between W and $W + dW$. These distributions are of particular interest as they elucidate the amount of energy available, how often it is released, and in which events and form (thermal or nonthermal) it predominantly occurs. The energy release observed in normal-size flares is not sufficient to constantly and consistently heat the corona to the observed few million kelvins. So the question is then whether this could be achieved by extending the observed flarelike energy releases to smaller scales. This concept can be expressed in terms of the power-law index of this distribution: if $\alpha \geq 2$, then the smallest events have a high occurrence rate and their energy dominates over larger flares, possibly matching the energy in coronal heating (Hudson 1991). This requires the assumption that these distributions be continuous into the unobservable low-energy range, which is difficult to determine as there are instrumental and selection effects that both cut off and bias the observed distribution (Aschwanden & Parnell 2002).

The instantaneous thermal energy in these events may be calculated from

$$W_T = 3n_e k_B TV, \quad (2)$$

where n_e is the electron density, V the volume of the emitting thermal plasma, k_B Boltzmann’s constant, and T the temperature. An estimate of the volume can be obtained by imaging the events; however, there can be an overestimate in this observed volume to the true volume by a filling factor $f \approx 1$ to 10^{-4} (Cargill & Klimchuk 1997; Takahashi & Watanabe 2000). In this work we assume $f = 1$, which will be discussed later. The temperature and emission measure may be found either directly from the spectrum or by imaging with different wavelength filters. Assuming constant density, the emission measure is related to the density and volume as $EM = n_e^2 V$, and so the thermal energy is

$$W_T = 3\sqrt{EMV} k_B T. \quad (3)$$

Note that as losses are not taken into account here, the energy going into the thermal plasma will be larger. For the smallest events this thermal energy has been found using pixelated detectors in EUV and soft X-rays, with simultaneous pixel brightenings within some area being registered as an event (Shimizu 1995; Krucker & Benz 1998; Aschwanden et al. 2000; Parnell & Jupp 2000; Aschwanden & Parnell 2002; Benz & Krucker 2002). The area inferred from these often spatially discontinuous, brightened pixels gives an estimate of the volume, and observations using different filters give temperature and emission measure information.

The events observed in EUV are termed “nanoflares” as they have about 10^{-9} times the energy in large flares, the limit of their

¹ Physics Department, University of California at Berkeley, Berkeley, CA 94720-7450.

observability being down to 10^{24} erg (Aschwanden et al. 2000). Parker's hypothetical nanoflare (Parker 1988) is an estimate of the basic unit of a localized impulsive burst of energy release, with energies $<10^{24}$ erg, with ensembles of them constituting the observed events. The thermal energy of these events outside of active regions has been investigated in soft X-rays with the *Yohkoh* soft X-ray telescope (SXT; Krucker et al. 1997) finding energies of 10^{25} erg per event, and in EUV using the *SOHO* EUV Imaging Telescope (EIT; Krucker & Benz 1998; Benz & Krucker 2002) and *TRACE* (Parnell & Jupp 2000; Aschwanden et al. 2000), providing energies between 10^{24} and 10^{27} erg. Small events in active regions, termed "active region transient brightenings," were seen in soft X-rays with *Yohkoh* SXT (Shimizu 1995), with energies between 10^{26} and 10^{29} erg. All of these studies found the power-law index of the frequency distributions to be between $\alpha = 1.5$ and -2.6 . Aschwanden & Parnell (2002) investigated the effect of instrumental bias on the different indices from *SOHO* EIT, *TRACE*, and *Yohkoh* SXT data. Parnell (2004) later pointed out that the discrepancy between power-law indices from different instruments can be due to the effects of least-squares fitting some of the binned histograms. Similar indices were obtained when a maximum likelihood method (Parnell & Jupp 2000) was used instead.

The nonthermal hard X-ray emission is assumed to be due to a power-law distribution of electrons emitting hard X-rays via bremsstrahlung in a thick target. The resulting power-law photon spectrum reflects this electron distribution (Brown 1971), allowing the power in these accelerated electrons above a low-energy cutoff E_C (in keV) to be calculated as

$$P_N(\geq E_C) = 9.5 \times 10^{24} \gamma^2 (\gamma - 1) \beta \left(\gamma - \frac{1}{2}, \frac{3}{2} \right) I_0 E_C^{(1-\gamma)} \text{ erg s}^{-1}, \quad (4)$$

where γ and I_0 are the index and normalization of the photon power-law spectrum (in units of photon flux, $\text{s}^{-1} \text{ cm}^{-2} \text{ keV}^{-1}$) and $\beta(m, n)$ is the beta function (Brown 1971; Lin 1974). Therefore, observing the hard X-ray spectrum of these events for various time intervals during each flare is sufficient to obtain an estimate of the nonthermal energy. However, there is ambiguity in the low-energy cutoff, E_C , because the observed photon spectrum depends only weakly on it, with a resulting flattening of the photon spectrum below ϵ_B not uniquely related to E_C , with $\epsilon_B \leq E_C$ (Holman 2003). Uncertainty in E_C results in a larger uncertainty in the power estimate: a factor of 2 increase/decrease in E_C would result in a factor of 8 decrease/increase in the power for flat spectra ($\gamma = 4$) or a factor of 64 decrease/increase in the power for steep spectra ($\gamma = 7$).

Previous statistical studies of the nonthermal energy in flares used the energy threshold of the instrument as an estimate of E_C , as they did not observe to low enough energies nor had sufficient energy resolution to observe the flattening of the spectrum. Crosby et al. (1993) using the *SMM* hard X-ray burst spectrometer (HXRBS) estimated the nonthermal energy in large flares >25 keV, finding that the power distribution at the peak time of emission had a power law with $\alpha = 1.67$ over 10^{27} – 10^{30} erg s^{-1} and the total nonthermal energy of these events had $\alpha = 1.53$ over 10^{27} – 10^{32} erg. Microflares were observed down to 8 keV with *CGRO* BATSE (Lin et al. 2001), finding energies over 10^{27} – 10^{30} erg, and by *GRANAT* WATCH down to 10 keV (Crosby et al. 1998).

RHESSI (Lin et al. 2002) is uniquely suited to investigate both the energy in the heated and accelerated electron populations,

thermal and nonthermal emission, of these small events. This is due to its unprecedented sensitivity to 3–25 keV X-rays, high spectral resolution, and imaging capabilities (Krucker et al. 2002). Previous studies of *RHESSI* microflares have concentrated on individual events (Krucker et al. 2002; Benz & Grigis 2002, 2003) or small samples, often compared to other wavelengths (Liu et al. 2004; Qiu et al. 2004; Battaglia et al. 2005; Kundu et al. 2005, 2006; Stoiser et al. 2008).

Here we present the first analysis of all *RHESSI* microflares found as transient bursts in 6–12 keV during periods of shutter-out observations, as detailed in Christe et al. (2008, hereafter Paper I). Between 2002 March and 2007 March, 25,705 events were found. These are active-region phenomena of low *C GOES* class to below A class. For the analysis presented here we measure the energy for 16 s around the time of peak emission in 6–12 keV. The peak time is only used as it presents the best opportunity to obtain enough counts above background to permit analysis in each event. Given the standard flare-time profile of a sharp impulsive rise followed by slower decay phase, this means that this analysis will mainly cover the impulsive phase of these microflares.

The calculation of the thermal energy using equation (3) requires knowledge of the volume of the thermal source and thermal parameters from the spectrum. Imaging these events, and hence estimating the volume of thermal emission, is detailed in § 2. In § 3 the spectral fitting of the events is described, obtaining the thermal and nonthermal parameters of these events. The relationship between these parameters and those found using *GOES* data are discussed in § 3.3. The calculation of the thermal energy and power in nonthermal electrons and the resulting frequency distributions is presented in § 4. We discuss these results further, including how this analysis at peak time relates to the emission over the whole of the microflare, in § 5.

2. IMAGING USING VISIBILITIES

RHESSI imaging is achieved through a Fourier-based method using rotation modulation collimators (RMCs; Hurford et al. 2002). Each RMC time-modulates sources whose size scale is smaller than its resolution. This spatial information encoded in the time-modulation profile is normally reconstructed into an image via techniques such as back projection (Hurford et al. 2002).

A recently implemented alternative technique converts the time-modulation profile to complex visibilities before recovering the spatial information (Hurford et al. 2005). Each *RHESSI* visibility is a calibrated measurement of a single Fourier component of the source distribution measured at a specific spatial frequency, energy, and time range. The visibilities are the complex quantities obtained from the fitted amplitude and phase of the modulated time profile for a particular roll orientation (rotational phase) of an individual RMC. The resulting set of visibilities for all roll angles and RMCs is a calibrated and compact representation of the original time profile, with little loss of information.

The advantage of using visibilities is twofold. First, as a smaller data set has to be processed, the image reconstruction from the visibilities is considerably quicker than using the time profile directly. Second, the visibilities are fully calibrated measurements, representing an intermediate step between the modulation profile and imaging, meaning that spatial information can be found directly from the visibilities without having to compute an image. This has been implemented in a Visibility Forward Fit (VFF) algorithm (Hurford et al. 2005) that determines the best-fit parameters, with statistical errors, for simple assumed source geometries (elliptical Gaussian, curved elliptical Gaussian, multiple sources, etc.).

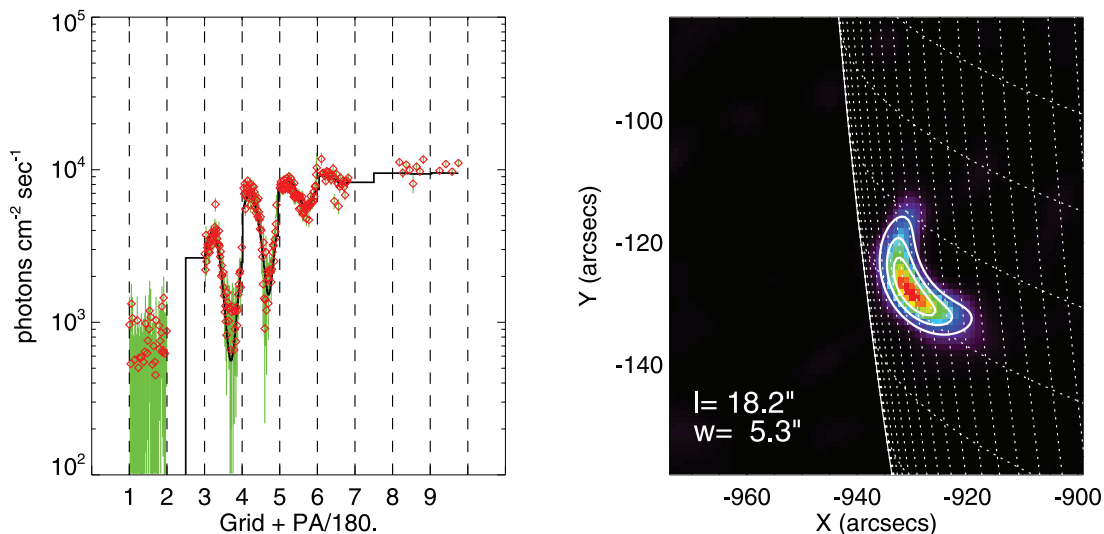


FIG. 1.—*Left*: Visibility forward-fit model loop shape (solid line) onto the 4–8 keV visibilities amplitudes (diamonds with error bars) as a function of the phase for each grid. The amplitudes for each grid/subcollimator are shown between the dashed vertical lines, indicating the amplitudes measured as the grids rotate from a position angle of 0° – 180° . Thus, an amplitude measured in subcollimator 3 when rotated to a position angle of 45° would be plotted against 3.25 on the x-axis. *Right*: Resulting image of the visibilities shown in the left panel. Background image found using MEM NJIT algorithm (Schmahl et al. 2007), with overplotted contours (25%, 50% and 75%) representing the model shape. The loop length l and width w are quoted.

We are primarily interested in the size of the thermal source, in order to make an estimate of the density and hence thermal energy (see § 4). The images of thermal sources in microflares are taken over 4–8 keV and generally have a single elliptical source or loop shape. We fit a two-dimensional (2D) model of a curved elliptical Gaussian to the 4–8 keV visibilities for 16 s about the peak in 6–12 keV for each microflare. This attempts to fit a Gaussian profile along the curved semimajor axis, equivalent to the loop arc length. If the source is not appreciably curved, an elliptical geometry of zero curvature is returned. Seven parameters are obtained from each fit of this 2D model: the centroid position (x , y), photon flux, FWHM loop length and width, curvature, and position angle of the semimajor.

An example of this fitting is shown in Figure 1. Here in the left panel we have the visibility amplitudes, with statistical errors, for each grid and its position angle. The solid line is the VFF model loop shape, which has fitted subcollimators 3, 4, 5, 6, 8, and 9 well. For this event the finest subcollimator, 1, is dominated by noise and so has little influence on the fit. Subcollimators 2 and 7 are not included as they provide a poor response in this energy range. The right panel shows the resulting image of these visibilities, produced using the MEM NJIT algorithm (Schmahl et al. 2007), with the VFF model loop from the left panel overplotted as contours. The contours correspond well with the background image. Further examples of the resulting fits are shown in Figure 2, again calculated using detectors 1, 3, 4, 5, 6, 8, and 9.

The model fit for each of the microflares not only provides the spatial information but also a measure of the “quality” of the fit, based on whether the fit converged, whether the fit parameters reach the limit of their range, and the size of the errors relative to the parameter. Such an objective measure of the fit quality is vitally important for an automated analysis project as it is impractical to visually inspect over 25,000 images. After processing all microflares, we have 18,656 microflares to which the model achieved a satisfactory fit and were resolved, i.e., returning spatial sizes larger than the instrumental resolution, $2.3''$. The majority of events producing poor fits were those that had the fewest counts. This can be seen in Figure 3, where the histogram of the 4–8 keV count rate per detector of all the microflares is shown,

as well as for the subsets of events producing good and bad fits. There are some microflares with large count rates but poor fits. This is likely due to an instrumental issue, such as to an absence of spacecraft roll information.

The histograms of the loop FWHM arc length l and width w (at loop midpoint) for the events with good VFFs are shown in Figure 4. We find that the median FWHM loop arc length is $31.6''$ (23 Mm) and width is $10.5''$ (8 Mm). The lengths’ distribution has a sharp peak, symmetrical in log-space, away from the resolution limit. The histogram of the ratio of the loop arc length to width (Fig. 4, middle panel) shows that the majority of the microflare thermal sources are elongated structures, with the median value of the arc length being 3 times the loop width. The size of these loops shows no correlation with the magnitude of the flare, either the flux in the loop or the background-subtracted GOES class (Fig. 5). This highlights that small flares are not necessarily spatially small, which is certainly the case for the examples shown in Figures 1 and 2.

The volume of this thermal emission can be estimated by assuming that the observed 2D loop structure has a cylindrical geometry as

$$V = \pi \left(\frac{w}{2} \right)^2 l, \quad (5)$$

where l is the FWHM loop arc length and w is the width at the loop midpoint. The histogram of the loop volume for the good events is shown in the right panel of Figure 4. The median volume is about $1 \times 10^{27} \text{ cm}^3$, which is a factor of ≈ 66 larger than the minimum measurable volume of $1.5 \times 10^{25} \text{ cm}^3$, found by taking $w = l = 2.3''$ in equation (5).

We obtain other useful parameters from VFF, in particular a measure of the total 4–8 keV photon flux from the loop. Since unmodulated background does not affect the visibilities, this flux measure is intrinsically background-subtracted as it is the emission from only the loop. In Figure 6 we have the differential frequency distribution of this 4–8 keV photon flux. This distribution covers a range of 5–5000 photons $\text{s}^{-1} \text{ cm}^{-2} \text{ keV}^{-1}$, and power-law parameters were found using a maximum likelihood

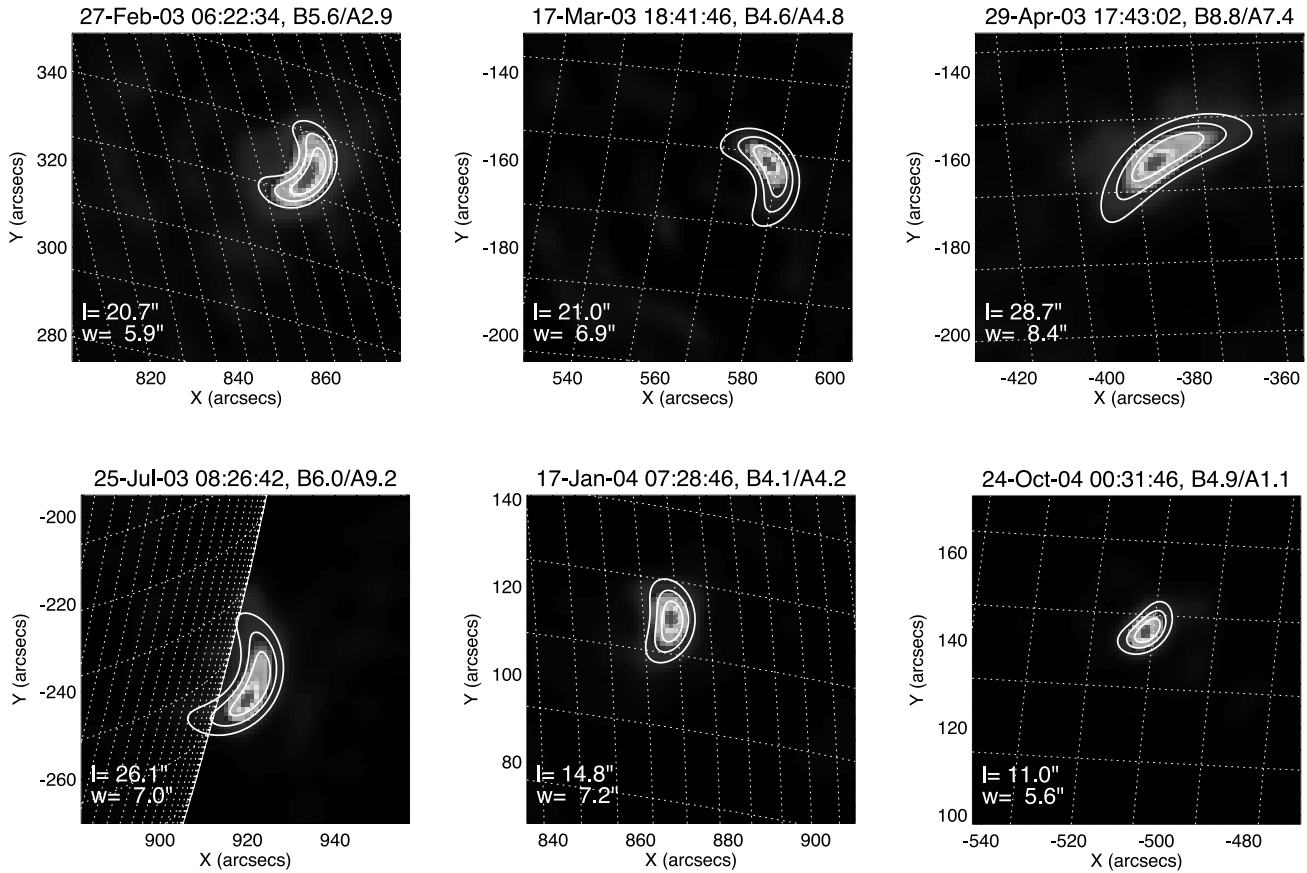


FIG. 2.— Example microflares showing the MEM NJIT image (*background*) and the forward-fit model shape (*foreground contours of 25%, 50%, and 75%*). The model loop length l and width w are quoted in each panel. [See the electronic edition of the *Journal* for a color version of this figure.]

method (Parnell & Jupp 2000). This technique uses the standard statistical procedure of the maximum likelihood estimation to fit a skew-Laplace distribution to the data. This distribution consists of a broken power law; the index above the break is the true distribution, whereas below it the power law fits the flattening/turning over of the distribution from undersampling the smallest

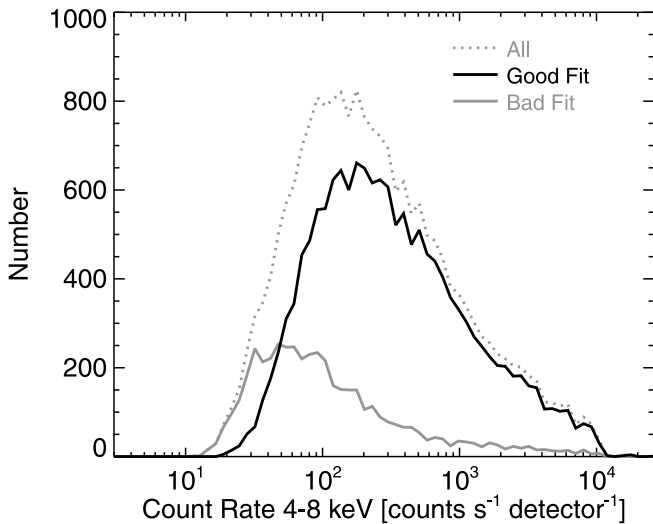


FIG. 3.— Histogram of the count rate per detector in 4–8 keV, the different lines indicating all microflares (*light gray dotted line*) and subsets with a good (*solid black line*) and bad (*solid gray line*) model fits to the visibilities.

events. So from a simple calculation on the sample (in this case 4–8 keV fluxes) an objective measure is obtained of the power-law index above a break (with errors found from the 95% sample confidence) instead of subjectively choosing bin sizes before line-fitting a histogram. For simplicity, the resulting fit is shown overplotted to a standard histogram in Figure 6. Over 2 orders of magnitude the power-law index is 1.71 ± 0.02 . This is steeper than the index of 1.59 found for hard X-rays >25 keV (Crosby et al. 1993) but flatter than that found for soft X-rays, 1.7–2.1 (Drake 1971; Lee et al. 1995; Feldman et al. 1997; Veronig et al. 2002). The distribution in Figure 6 deviates from a power law at both low and high fluxes due to instrumental selection effects. The events with the smallest and largest fluxes are missing as we are unable to successfully analyze these events: the smallest are hard to observe above background and the largest have excessive counts causing high detector deadtime or are excluded from our microflare list as *RHESSI's* attenuating shutters were deployed.

Another way in which we can use this *RHESSI* 4–8 keV thermal flux is by comparing it to the emission observed by *GOES* in its 1–8 Å band (Fig. 7). Here we see that there is a power-law correlation, with index close to 1, although there is some spread about the fitted line. This suggests that *RHESSI* and *GOES* are observing the emission from the same thermal plasma with the different temperature distribution from event to event accounting for the spread in the correlation. In comparison to *RHESSI* quiet-Sun observations (Hannah et al. 2007), the smallest microflare flux measured here is over 2 orders of magnitude larger than the limit found from an active-region-free quiet Sun. The quiet-Sun *RHESSI* flux also correlates with the *GOES* flux with

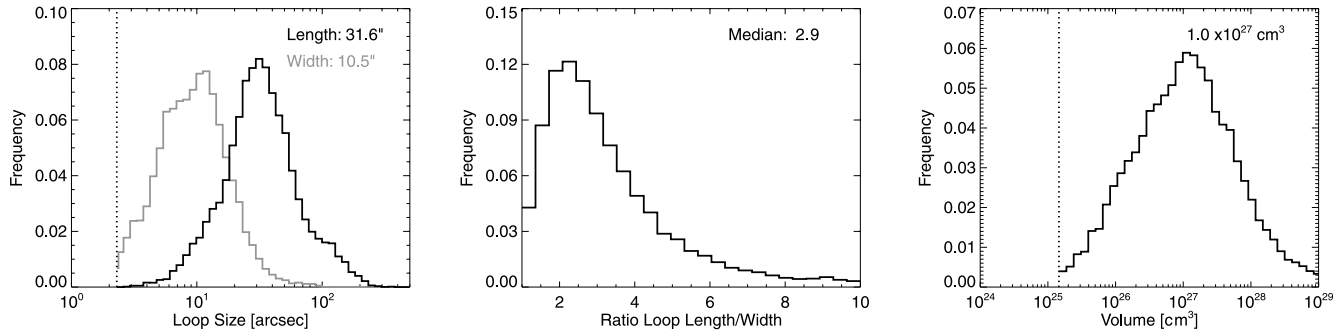


FIG. 4.—*Left*: Histogram of the model loop arc length and width for 18,656 *RHESSI* microflares. The dotted vertical line indicates the instrumental resolution limit of $2.3''$. *Middle*: Histogram of the ratio of 4–8 keV microflare loop length to width. *Right*: Histogram of the microflare volume of the 4–8 keV loops, assuming cylindrical geometry from the 2D fitted width and length. The dotted vertical line indicates the minimum measurable model volume.

a slightly steeper slope (1.08 ± 0.13) than the microflares shown here.

3. SPECTRUM FITTING

The spectrum of each microflare is determined over the same time period as the visibilities in § 2, 16 s around the time of peak

emission in 6–12 keV. These spectra are made with $\frac{1}{3}$ keV energy bins between 3 and 30 keV using detectors 1, 3, 4, 5, 8, and 9. For each microflare, a background interval before and after the event were determined automatically with the selection of these background times described in Paper I. Only the preflare background is used in the subtraction from the spectrum, as it is sharply defined by the microflare’s impulsive phase. This was possible for 19,441 microflares. The histogram of the flare signal-to-background ratio is shown in Figure 8, for the 6–12, 4–8, and 12–16 keV energy bands. Requiring the flare signal to be at least 3 times the preflare background, we find 12,814 events suitable in 6–12 keV (the energy range the events were found in), 12,472 in 4–8 keV from predominantly thermal emission, and 9681 in 12–16 keV from mostly nonthermal emission. This indicates that the thermal component for more microflares can be obtained than the nonthermal component. This does not mean that many microflares do not have a nonthermal component, just that we cannot distinguish it from the background in these cases.

These background-subtracted observed count spectra are forward-fitted with a model in photon space converted back to count space using the full *RHESSI* detector response matrix (Smith et al. 2002) in the OSPEX software package, an updated version of the SPEX code (Schwartz 1996). The model has both a thermal and nonthermal component so that we can recover the respective parameters to calculate the energy in both the heated

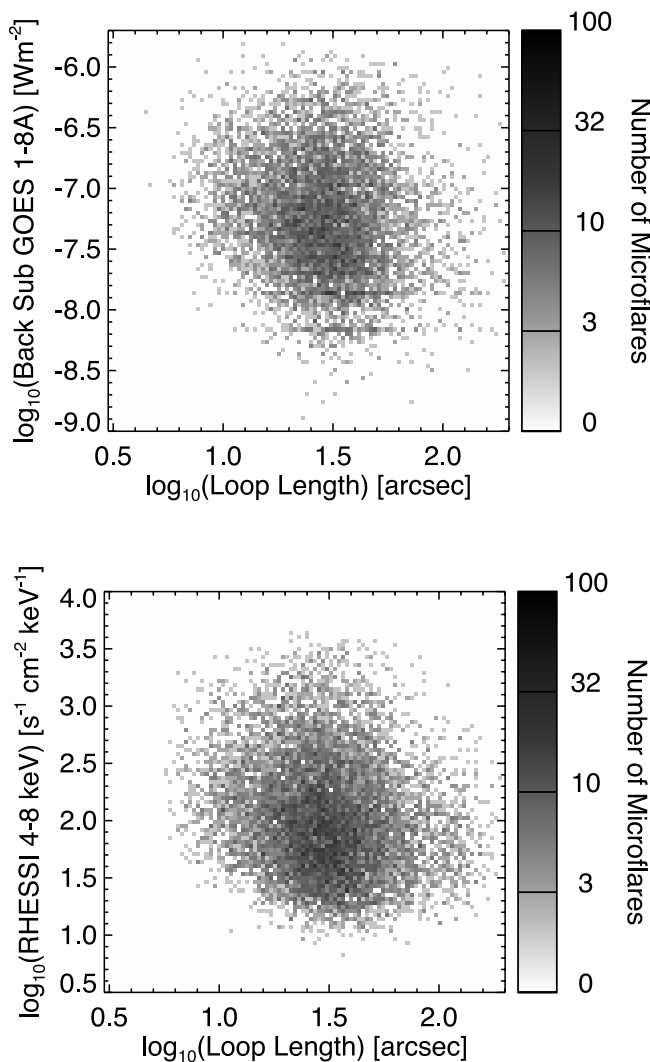


FIG. 5.—Correlation plots of the model loop arc length against the background-subtracted *GOES* 1–8 Å soft X-ray flux (*top*) and the *RHESSI* image model’s 4–8 keV flux (*bottom*). [See the electronic edition of the *Journal* for a color version of this figure.]

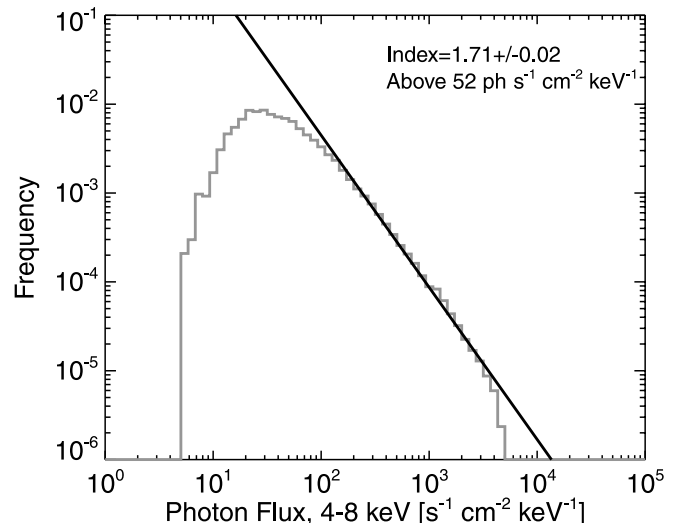


FIG. 6.—Frequency distribution of the total photon flux measured from the VFF 4–8 keV loops. The power-law fit is performed using a maximum likelihood method of Parnell & Jupp (2000) and is not a graphical fit to the histogram shown.

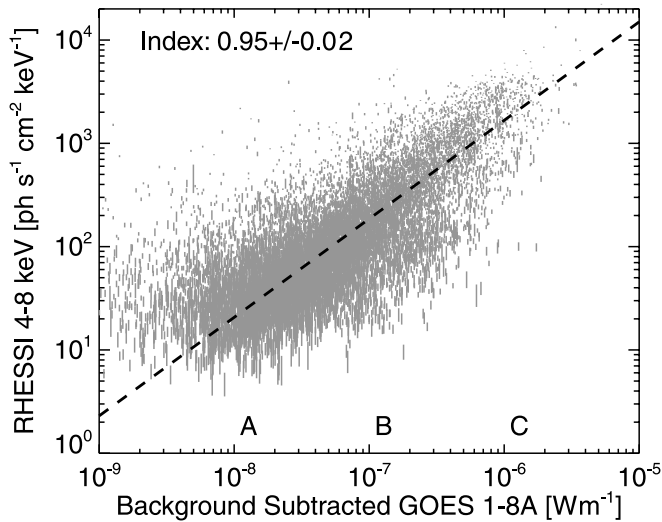


FIG. 7.—Background-subtracted *GOES* 1–8 Å soft X-ray flux against the *RHESSI* image model’s 4–8 keV flux.

and accelerated electrons. The thermal component contains the isothermal bremsstrahlung emission (free-free and free-bound) as well as line emission from the CHIANTI database (Dere et al. 1997; Landi et al. 2006). This emission depends on temperature T and emission measure $EM = n_e^2 V$. The nonthermal component is assumed to be thick-target emission of a power-law distribution of electrons above a low-energy cutoff E_C , with the photon spectrum found through numerical integration (Holman 2003). Although this numerical integration provides an accurate representation of the nonthermal emission, it is too slow to compute in this fitting procedure, requiring multiple iterations per microflare, with tens of thousands of microflares to fit. Instead, the nonthermal component is fitted with a broken power law, which has an index of $-\gamma$ above the break energy of ϵ_B and a fixed index of -1.5 below the break. An example of this approximation to the numerical integration is shown in the left panel of Figure 20, and the relationship between these two models is detailed further in § 4.2, as it is important for calculating the power in the nonthermal electrons via equation (4).

The fit to each microflare spectrum is conducted using the following strategy. First, the thermal parameters are varied to fit the spectrum over 4–8 keV, where the thermal emission normally dominates. Then the fit is repeated but the nonthermal parameters are allowed to vary, while keeping the previously found thermal parameters fixed, to fit the spectrum from 10 keV up to either 30 keV or the point at which the background dominates over the flare signal. The fit is repeated a final time, allowing all the fit parameters to vary to fit the spectrum from 3 keV up to either 30 keV or the point at which the background dominates over the flare signal. Examples of typical microflare spectra and the fits are shown in Figure 9. The microflares here illustrate similar characteristics as seen in previous *RHESSI* microflare studies, for example, Krucker et al. (2002). At low energies (≤ 10 keV) the thermal component dominates with the expected spectral lines, Fe K-shell feature (about 6.7 keV), and the Fe/Ni lines (about 8 keV), for this temperature range (Phillips 2004). At higher energies (≥ 10 keV) there is a power-law component that dominates over the thermal model that is normally assumed to be the nonthermal emission. Although this could be an additional hotter thermal component, several other arguments imply nonthermality: the presence of the Neupert effect (Benz & Grigis 2002) in some cases, imaged hard X-ray footpoints (Krucker et al. 2002), and

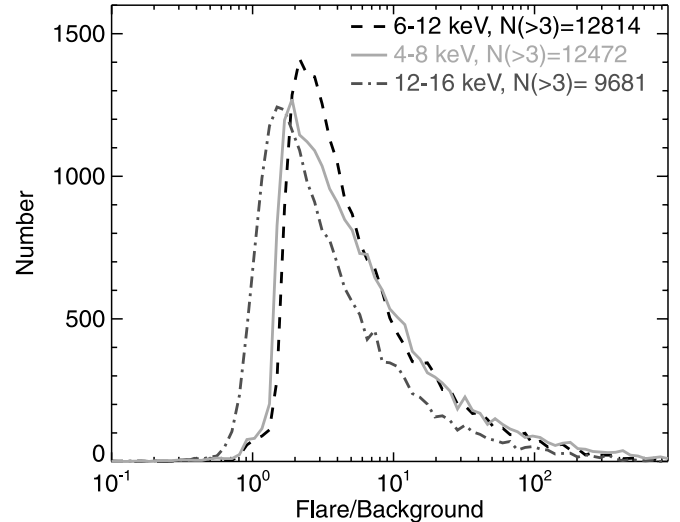


FIG. 8.—Histogram of the ratio of flare signal to preflare background in 6–12 keV (dashed line), 4–8 keV (solid line), and 12–16 keV (dash-dotted line) at the time of peak emission in 6–12 keV.

complementary radio and microwave observations (Liu et al. 2004; Qiu et al. 2004; Kundu et al. 2005, 2006).

As with the imaging, the spectral fitting returns parameters that objectively measure the quality of the fit, such as the fit χ^2 or whether the fit parameters have large errors or reach the limit of their chosen fitting range. We obtain 9161 events for which we trust the fit to the thermal component of the spectrum and the forward-fit model loop. This is out of a possible 9693 microflares with good background subtraction, flare signal-to-background ratio over 4–8 keV, and a successful model fit. For the thermal and nonthermal fits as well as the VFF model loop fit to the visibilities we obtain 4236 trustworthy events. This is out of a possible 8046 microflares with good background subtraction, flare signal-to-background ratio over 10–12 keV, and successful model fit. The histograms of these fitted parameters are shown in Figure 10 and discussed in §§ 3.1 and 3.2.

3.1. Thermal Parameters

The histograms of the fitted temperature and emission measure for the events with good background subtractions and thermal fits, 9161 microflares, are shown in the top row of Figure 10. This is about a third of the total sample but shows nearly all of the events with good background subtraction, flare signal-to-background ratio, and visibility forward fits (9693 microflares). The majority of the temperatures found lie within a tight range of ~ 10 – 15 MK, with the median temperature of ~ 13 MK. The emission measures vary considerably more than the temperatures, having a range covering over 2 orders of magnitude between 10^{45} and 10^{47} cm^{-3} . The median emission measure is 3×10^{46} cm^{-3} . Also shown in Figure 10 is the average ratio of the error in the fit to the fitted parameter. For the temperatures this statistical error in the fit is $< 1\%$ and is approximately constant for the temperatures found. The error in the emission measure is $\approx 10\%$ at 10^{45} cm^{-3} but drops to $\approx 1\%$ at 10^{47} cm^{-3} . The larger relative error in the events with smallest emission measure is due to the emission measure being directly proportional to the thermal emission model, and so are events with small noisy spectrum. The range of these parameters is discussed further in § 3.3. With these emission measures and the volumes of the emitting plasma (see § 2) an estimate of the electron density can be made. The histogram of these densities is shown in Figure 11 and range from 6×10^8 to 6×10^{10} cm^{-3} with

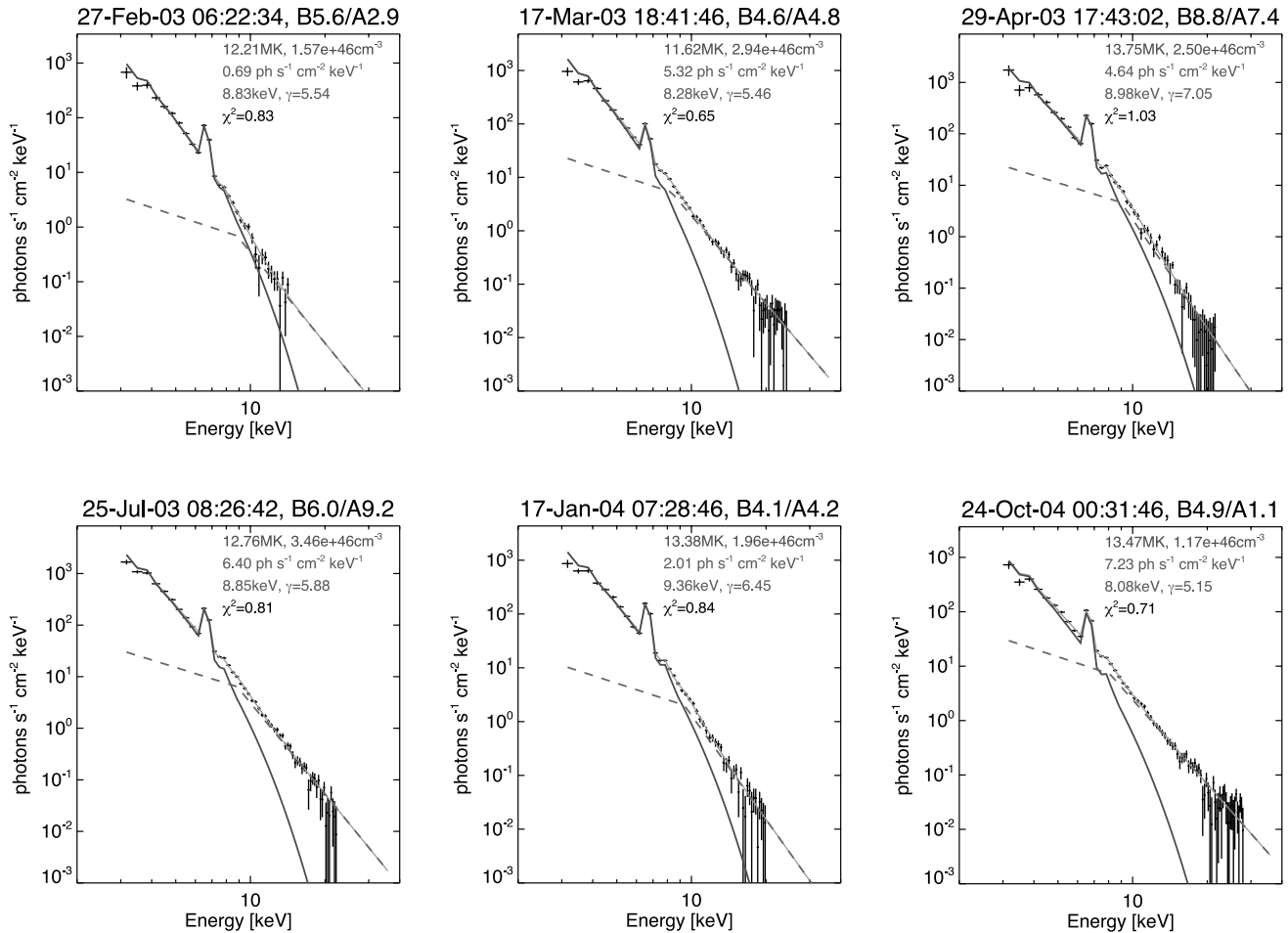


FIG. 9.— Example microflare spectra. Shown are the background-subtracted data (black plus signs), thermal model (black solid line), nonthermal model (dashed line) and total model (gray solid line). The title shows the GOES class and the background-subtracted equivalent. [See the electronic edition of the Journal for a color version of this figure.]

a median value of $6 \times 10^9 \text{ cm}^{-3}$. This is larger than typical coronal conditions but reasonable for a flaring loop (Phillips et al. 1996; Gallagher et al. 1999).

With these fitted thermal components we can estimate the 4–8 keV flux from these spectrum fits and compare it to the flux derived from the imaging in § 2. This provides a consistency check to verify that these two vastly different analysis techniques recover similar fluxes. The histogram of the ratio of the flux found from the spectrum model to the image value is shown in Figure 12. The median of these is 1.0 with some spread about this value. This is expected as different detectors were used for imaging and spectral analysis (additional use of detector 5 in imaging), and the imaging calculation uses only the diagonal elements of *RHESSI*'s detector response matrix (Smith et al. 2002), whereas the spectrum fitting uses the full response matrix.

3.2. Nonthermal Parameters

Histograms of the index γ and break energy ϵ_B of the nonthermal broken power law are shown in the bottom row of Figure 10. The power-law index γ has values mostly ranging over 4–10 with the median about 7. This is considerably steeper than large flares observed by *RHESSI*, as discussed in previous *RHESSI* microflare work (Krucker et al. 2002; Benz & Grigis 2002). The break energy ϵ_B ranges over 7–12 keV with the median being about 9 keV, which is smaller than that found for larger flares (Saint-Hilaire & Benz 2005). In larger flares, the lower energy

nonthermal emission would be masked by the thermal emission to tens of keV. The steep power laws starting at low energies lead to a strong selection effect. This is because such steep power laws, extending down to energies where there are spectral lines (Phillips 2004), are difficult to distinguish from a thermal component. A conservative approach has been taken here to remove any events where there is an ambiguity between the thermal and nonthermal components, so we discount any events with $\epsilon_B \leq 7$ keV. The result is that we have only 4236 microflares, about a fifth of the total sample.

Also shown in Figure 10 are the average ratios of the error in the fit to the fitted parameter. For the power-law index γ this statistical error in the fit is $\approx 4\%$ for $\gamma < 8$ and increases to $\approx 10\%$ for $\gamma > 8$. This increase in the error shows the greater uncertainty in trying to fit steep spectrum. The error in the break energy is $\approx 10\%$ at about $\epsilon_B = 7$ keV and decreases to $> 1\%$ by $\epsilon_B = 12$ keV. The large errors at low break energies show the greater uncertainty in trying to separate the thermal and nonthermal components below 10 keV. These nonthermal parameters are discussed further in § 4.2.

3.3. Correlation between Parameters

Figure 13 plots the temperature against emission measure for the *RHESSI* microflares. There is no clear correlation between these parameters. Also shown are numbered contours indicating constant count rate per detector over 4–8 keV for the thermal

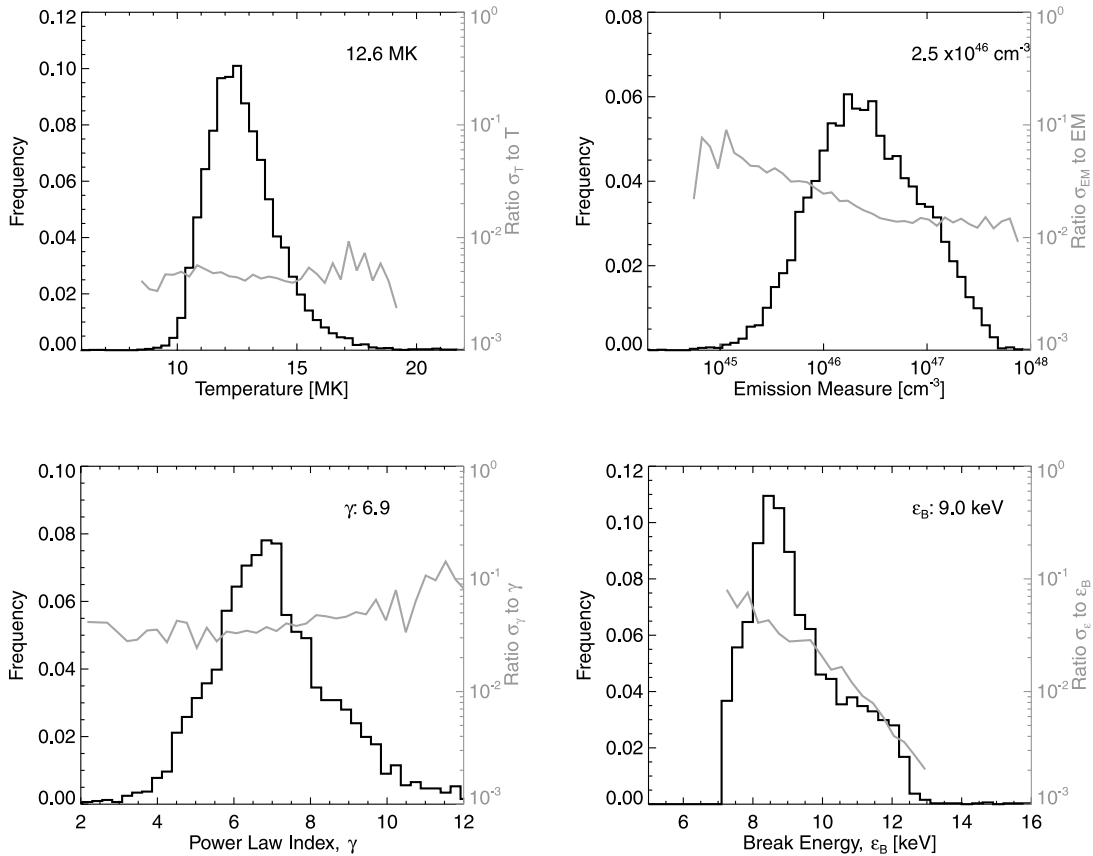


FIG. 10.—*Top*: Histogram of the microflare temperature (*left*) and emission measure (*right*) from the spectral fits of 9161 *RHESSI* microflares. *Bottom*: Histogram of the photon power-law index γ (*left*) and break energy ϵ_B (*right*) for 4236 *RHESSI* microflares. The gray lines in each panel refer to the right-hand axis and show the average ratio of the error in the fit to the fitted parameter, as a function of the parameter.

model as a function of temperature and emission measure. All of the microflares lie between the 10 and 10^4 counts s^{-1} contours, consistent with the non-background-subtracted count rates for good fits shown in Figure 3. Although any temperature and emission measure between these contours could be expected, the temperatures lie in a tight range, mostly between 10 and 15 MK, with almost all possible emission measures, from 10^{45} to 10^{47} cm^{-3} , for this temperature range found. The model of the thermal

emission is directly proportional to EM and increases with larger T , although not directly, with the continuum rising and flattening and the line features becoming more prominent (Tandberg-Hanssen & Emslie 1988). This results in the errors in the temperature and emission measure being anticorrelated. The thermal model also includes spectral features, and they provide additional emission, particularly from the Fe K shell over 4–8 keV for temperatures above 8 MK (Phillips 2004). The fact that only

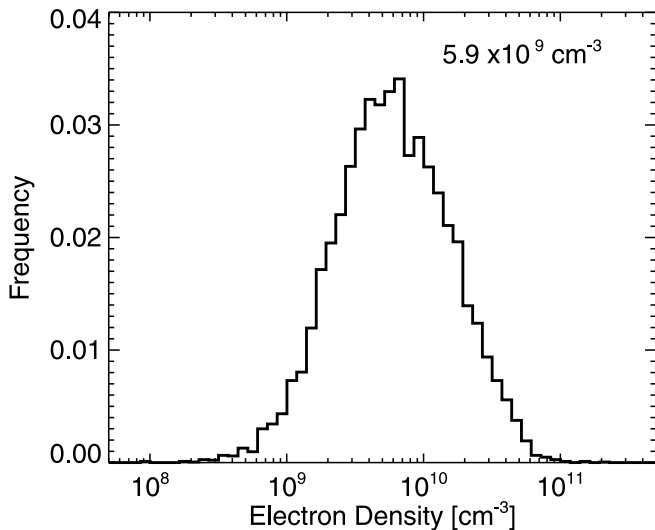


FIG. 11.—Histograms of the density of the 4–8 keV loops, found from the emission measure and thermal volume for 9161 *RHESSI* microflares.

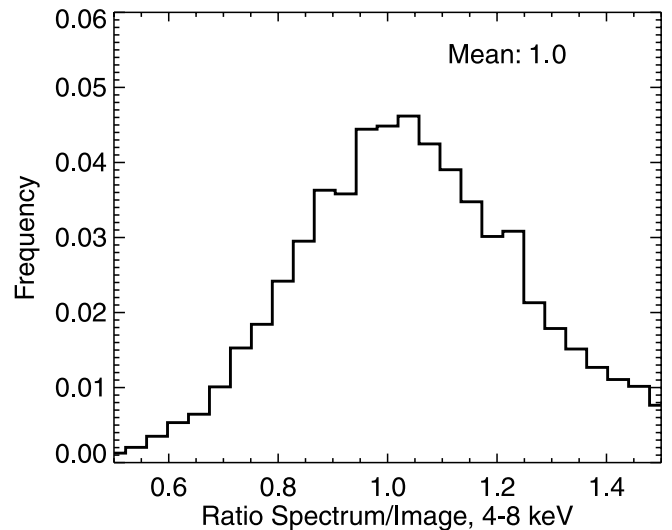


FIG. 12.—Histogram of the ratio of the 4–8 keV flux found from the fitted spectrum model and the image model loop.

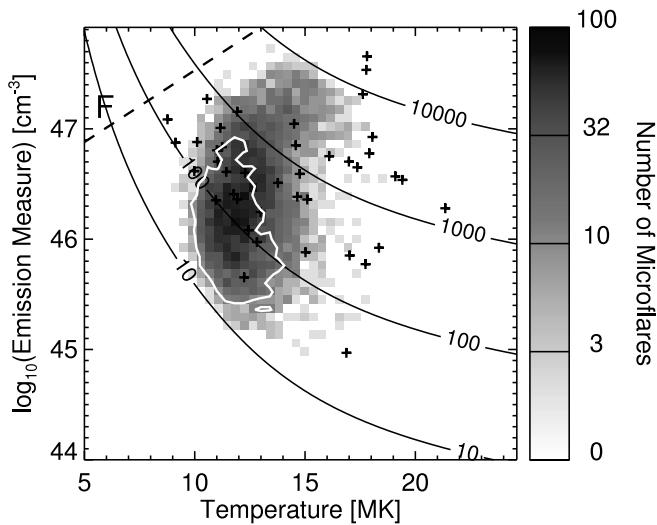


FIG. 13.— Microflare temperature against emission measure. The correlation plot is the microflares in this study with black plus signs representing the results of a previous *RHESSI* study (Battaglia et al. 2005). The dashed straight line represents the correlation found by Feldman et al. (1996b) from *GOES* and *Yohkoh* BCS. The numbered curved lines are of constant count rate per detector in 4–8 keV for the thermal model, as a function of temperature and emission measure. The white contour show the events that have a *GOES* temperature < 10 MK in Fig. 14. [See the electronic edition of the *Journal* for a color version of this figure.]

temperatures above 8 MK have been found is more suggestive of a selection effect primarily affecting the temperatures and not a physically significant discovery of microflares with a lack of low temperatures and high emission measures. This selection effect is consistent with *RHESSI*'s sensitivity being temperature-dependent. The combination of this greater sensitivity to hotter plasma and the differential emission measure (DEM) decreasing as the temperature increases could explain the tight range of temperatures found with the peak of this sensitivity for *RHESSI* shutter-out mode occurring in this temperature range. Note that this selection effect essentially does not reject any event detectable by *GOES*.

Microflares analyzed in a previous *RHESSI* spectral study of flares of all scales, 42 microflares out of a sample of 85 flares (Battaglia et al. 2005), are shown as plus signs in Figure 13 and also showed no correlation. These events specially chosen to cover a wide range of *RHESSI* flare magnitudes were analyzed during the peak in 12–25 keV. This is earlier in the flare phase than for our survey. Thus, they have correspondingly higher temperatures and lower emission measures. Another recent study of 18 microflares from a single active region (Stoiser et al. 2008) found similar results to the Battaglia et al. (2005) study.

The dashed line in Figure 13 is the correlation found using soft X-ray observations with *GOES* and *Yohkoh* BCS (Feldman et al. 1996b), for all size of flares from A through X class, not just microflares. This correlation has an order of magnitude spread in emission measure and only becomes apparent when a large range of flare magnitudes are included; for only small A-class events the correlation was in the opposite direction (Feldman et al. 1996a) with the emission measure decreasing with increasing temperature. In comparison, the *RHESSI* data, which is observed at higher energies than those in Feldman et al. (1996b), show higher temperature and/or lower emission measures. This is consistent with the DEM peaking at temperatures lower than those observed with *RHESSI* and closer to those lower temperatures observed by *GOES* and *Yohkoh* BCS. This was found to be the case for the DEM of a large flare observed in soft X-rays with *GOES* and *Yohkoh* SXT and in hard X-rays with *Yohkoh* HXT (Aschwanden

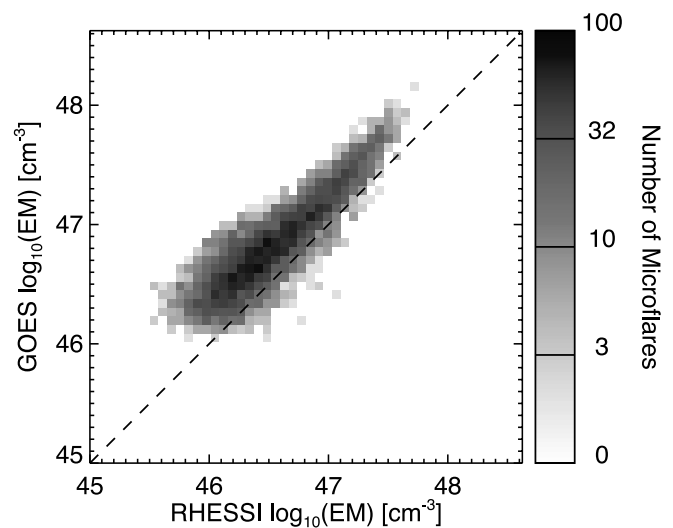
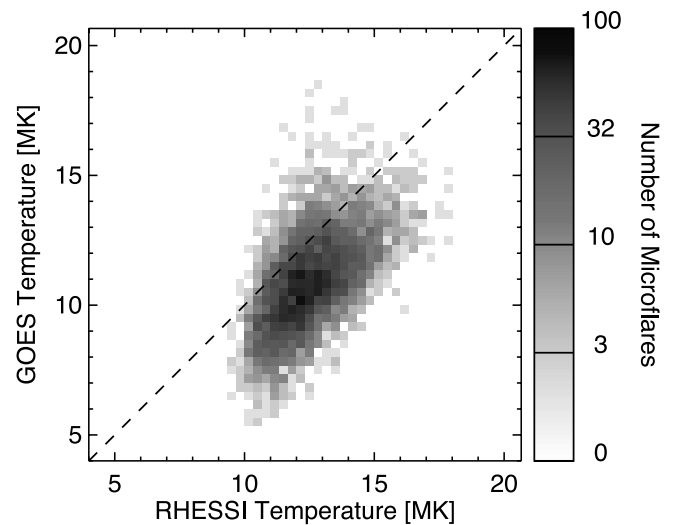


FIG. 14.— Correlation plots of temperature (*top*) and emission measure (*bottom*) from *RHESSI* and *GOES* for the same peak time in *RHESSI* 6–12 keV for 6740 microflares. The dashed lines indicate a one-to-one correlation. [See the electronic edition of the *Journal* for a color version of this figure.]

& Alexander 2001). For *RHESSI* emission measures above $8 \times 10^{46} \text{ cm}^{-3}$ there is the hint of a similar correlation with temperature, but it is obscured by the temperature selection effect at lower emission measures. Further studies of solar flare temperature and emission measure suggested that the emission measure of EUV nanoflares approximately scales as T^5 (Aschwanden et al. 2000), but using various studies over larger scales suggested the emission measure may scale as T^4 (Aschwanden 2007). These scalings are only approximate as there is large scatter about the correlation line. Looking over larger ranges with different instruments helps to reduce the overall influence of the selection effects, but there is still ambiguity as to how these parameters scale.

To gain a better understanding of the *RHESSI* temperature and emission measure, we have also calculated the *GOES* temperatures and emission measures for each of these microflares. This was done using the same preflare time for background and peak time of emission in 6–12 keV, as was used in the *RHESSI* analysis. This was possible for 6740 microflares, removing those events for which a *GOES* temperature and emission measure were not reliably calculable. The resulting correlation plots are shown in Figure 14. The bottom right hand of this correlation plot (the

lowest *GOES* temperature for each *RHESSI* temperatures) does seem to be directly proportional, except the *RHESSI* temperatures are about 5 MK higher. The rest of the plot is again dominated by the selection effect in the *RHESSI* temperatures. The events with *GOES* temperature < 10 MK have been highlighted by the white contour in Figure 13. If the assumption is that the *RHESSI* temperature estimate is too high in these events, and the emission measures are consequently too small, then this set of highlighted events should be moved upward and to the left in Figure 13. This shift produces a clearer hint of the previously found correlation between temperature and emission measure.

The emission measures in Figure 14 do not show any such temperature selection effect and are nearly directly proportional, with the *GOES* emission about twice that observed in *RHESSI*. Again, this will be due to *RHESSI* observing in a temperature range that is higher than the peak temperature in the DEM. The proportionality between the *RHESSI* and *GOES* emission measures on face value suggests a similarly steep DEM in all the microflares, but this might be arising from the relative instrumental sensitivities. It is important to remove these instrumental effects to recover the underlying DEM, but this is a complicated process and has only been successful for individual large flares (cf. Aschwanden & Alexander 2001).

Other studies (Feldman et al. 1996b; Battaglia et al. 2005) have also investigated how the temperature and emission measure relate to the *GOES* flux of the events. The *RHESSI* microflare temperature and emission measure plotted against each event's corresponding background-subtracted *GOES* 1–8 Å is shown in Figure 15. Again, there is a hint of a correlation between the *RHESSI* temperature and *GOES* flux for the events above B class (10^{-7} W m $^{-2}$), but it is obscured in smaller events again due to the temperature selection effect. The previous study of *RHESSI* flares (Battaglia et al. 2005) found a correlation when using large flares in addition to microflares. This correlation and the microflares in their sample are shown in Figure 15 by the dashed line and plus signs and is steeper than those found using *GOES* and *Yohkoh* BCS (Feldman et al. 1996b). The hint of a correlation in our microflare study scales in a manner closer to Feldman et al. (1996b) than Battaglia et al. (2005), although the temperatures found are consistently higher.

There is a clear correlation between the emission measure and *GOES* flux, which can be fitted as $F_G = 1.15 \times 10^{-52} EM^{0.96}$, with F_G in W m $^{-2}$ and EM in cm $^{-3}$. A similar result was also found in the Battaglia et al. (2005) study, fitted over a large flare to microflare range finding $F_G = 3.6 \times 10^{-50} EM^{0.92}$. The consistently lower emission measures in this study are again due to this analysis occurring earlier in the microflare than in our study.

We can also investigate how the nonthermal emission relates to the thermal parameters, which is shown in Figure 16. Here the nonthermal flux F_N , in units of photon flux at Earth s $^{-1}$ cm $^{-2}$ keV $^{-1}$, is taken from the fitted broken power-law parameters at 12 keV. This energy is used as it is above the break energy ϵ_B in all events but is still at an energy for which we observe nonthermal emission. Both the temperature and emission measure scale with the nonthermal emission. The correlation with the temperature is fitted as $T = 1.41 \log F_N + 13.2$, with T in MK. A similar correlation was found in the Battaglia et al. (2005) study using the flux at 35 keV for the nonthermal flux, since larger flares were also analyzed, finding $T = 1.46 \log F_{35} + 21.57$. We find that the scaling of the emission measure is flatter, $EM = 4 \times 10^{46} F_N^{0.57}$, than the previous study, $EM = 5 \times 10^{48} F_{35}^{0.91}$ (Battaglia et al. 2005); again, EM is in units of cm $^{-3}$.

In Figure 17 this nonthermal photon flux at 12 keV, F_N , is plotted against the model thermal flux over 4–8 keV, F_T . The

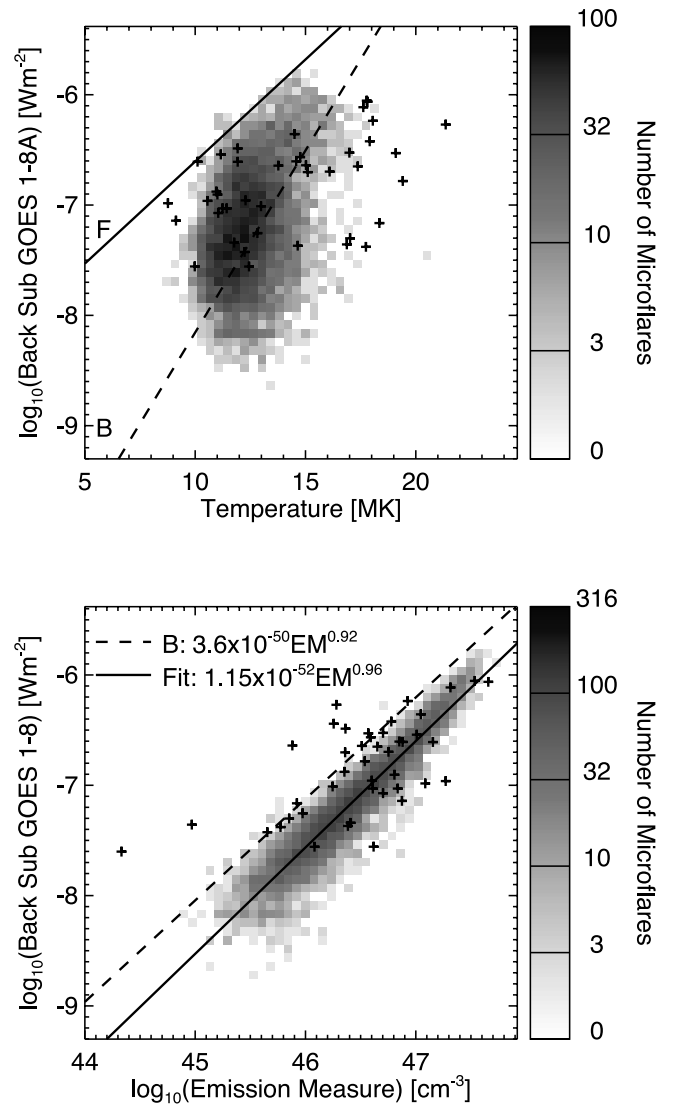


FIG. 15.—Microflare temperature (*top*) and emission measure (*bottom*) against the background-subtracted *GOES* 1–8 Å flux. The correlation plots are the microflares in this study, with the dot-dashed line (*bottom panel*) the fit to these data. The black plus signs and dashed line were found from a previous *RHESSI* study (Battaglia et al. 2005). The solid line (*top panel*) represents the correlation found by Feldman et al. (1996b). [See the electronic edition of the Journal for a color version of this figure.]

thermal and nonthermal emission correlate, with the fit being $F_N = 3.4 \times 10^{-3} F_T^{1.09}$, but with a greater scatter in the smaller events. At higher fluxes the correlation steepens, suggesting that there might a greater proportion of nonthermal emission relative to thermal emission in larger flares. However, this may just be an instrumental effect, arising from detector pileup and live-time issues in these larger events prior to the shutters deploying.

4. ENERGY DISTRIBUTIONS

4.1. Thermal Energy Frequency Distributions

Using the volumes found in § 2 and temperature and emission measure found in § 3, the thermal energy W_T , over the time of peak emission in 6–12 keV, can be calculated via equation (3). The energies range from 10^{26} to 10^{30} erg with the median being about 10^{28} erg. The frequency distribution (number of events per energy bin range, area of solar disk, and duration of observation period) of this energy for 9161 microflares is shown in Figure 18. The

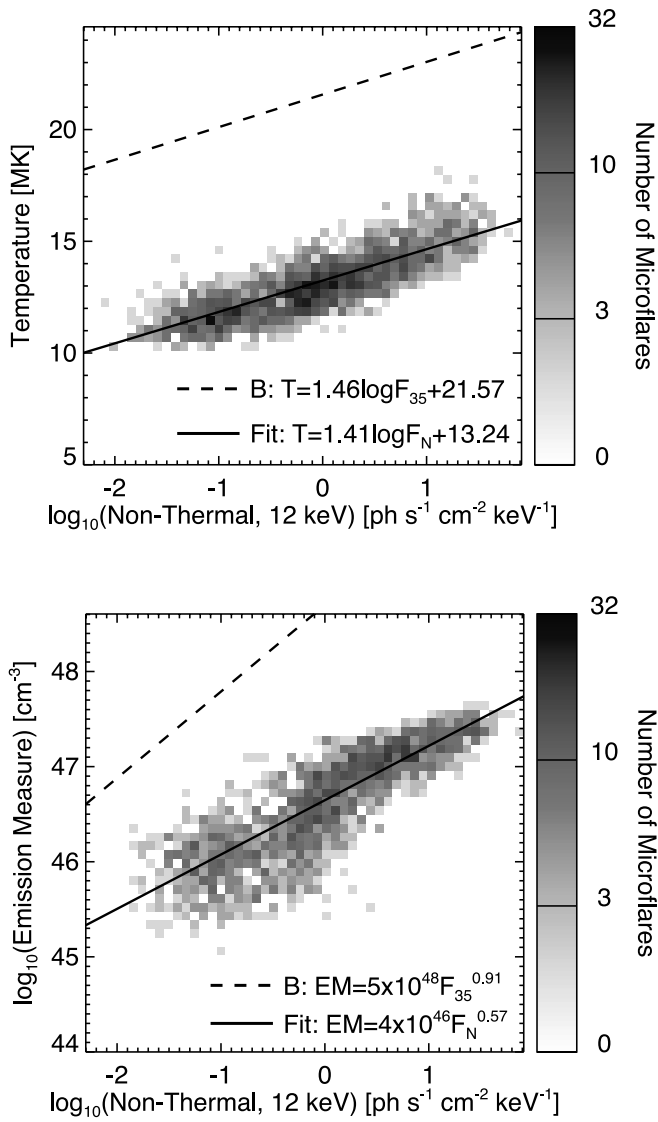


FIG. 16.—*RHESSI* nonthermal photon flux at 12 keV, from the fitted broken power law, against fitted temperature (*top*) and emission measure (*bottom*). The correlation plots are the microflares in this study; the fit to these data is the dot-dashed line. The dashed line is from a previous *RHESSI* study using the nonthermal flux at 35 keV (Battaglia et al. 2005). [See the electronic edition of the *Journal* for a color version of this figure.]

resulting *RHESSI* thermal energy distribution is not a clear power law; it has a turnover at low energies and steepens at higher energies. These features are instrumental effects due to missing the smallest events, with insufficient counts to either find the events or successfully analyze them, and the largest events, due to detector live-time issues before the attenuating shutters come in. Considerably more small events are missing than large, since the discrepancy from a power law is greater at lower energies than high. As this distribution deviates from a power law it will not be fitted to obtain the power-law index α . Instead, Figure 18 shows an $\alpha = 2$ line, indicating the parts of the *RHESSI* thermal distribution can be steeper and flatter, or larger and smaller, than $\alpha = 2$.

Compared to the previous distributions found for EUV nano-flares (Krucker & Benz 1998; Aschwanden et al. 2000; Parnell & Jupp 2000; Benz & Krucker 2002) and soft X-ray active-region transient brightenings (Shimizu 1995), the *RHESSI* energy distribution appears as an extension to these at higher energies. This

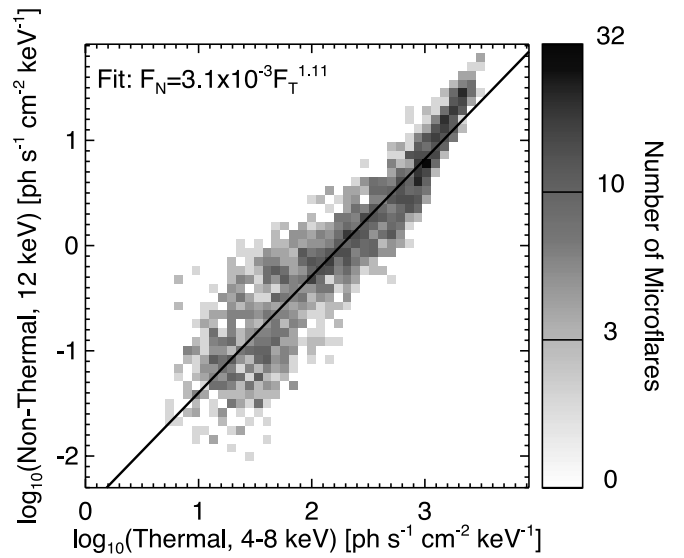


FIG. 17.—*RHESSI* nonthermal flux at 12 keV, from the fitted broken power law, against the thermal flux over 4–8 keV, from the thermal model. The dot-dashed line is the fitted correlation line. [See the electronic edition of the *Journal* for a color version of this figure.]

is both remarkable and deceptive since these distributions were found for very different types of events, using various instruments and for different periods during the solar cycle. For instance, the *SXT* energies (Shimizu 1995) are from 291 brightenings in one active region over 5 days in 1992 August, whereas the *EIT* (Krucker & Benz 1998; Benz & Krucker 2002) and *TRACE* EUV quiet-Sun observation (Aschwanden et al. 2000; Parnell & Jupp 2000) were found over about an hour each on 1996 July 12, 1998 February 17, and 1998 June 16, respectively. So there are two key issues that have to be taken into account when looking at the energy distributions in Figure 18. First, various instruments were used, so different components of the thermal energy will be observed and with distinctive instrumental selection effects will influence each distribution. This makes it difficult to determine whether these are similar events or completely distinctive

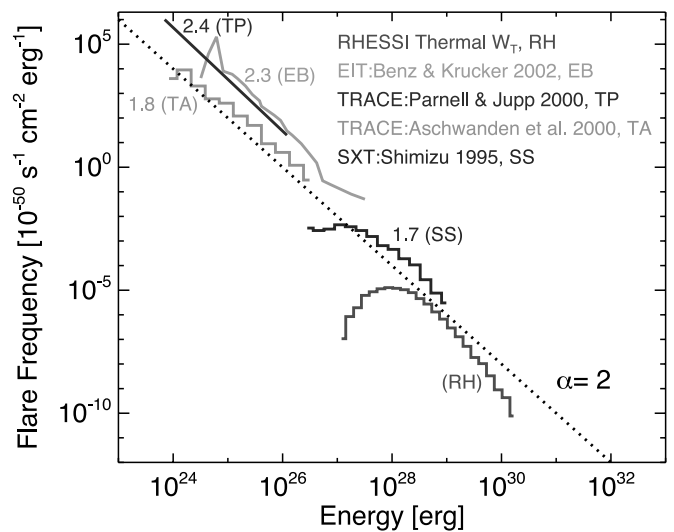


FIG. 18.—Frequency distribution of the thermal energy of 9161 *RHESSI* microflares (RH) in context of thermal energy distributions of nano-flares (TA, TP, and EB) and active region transient brightenings (SS). The dotted line indicates a power-law index of $\alpha = 2$. [See the electronic edition of the *Journal* for a color version of this figure.]

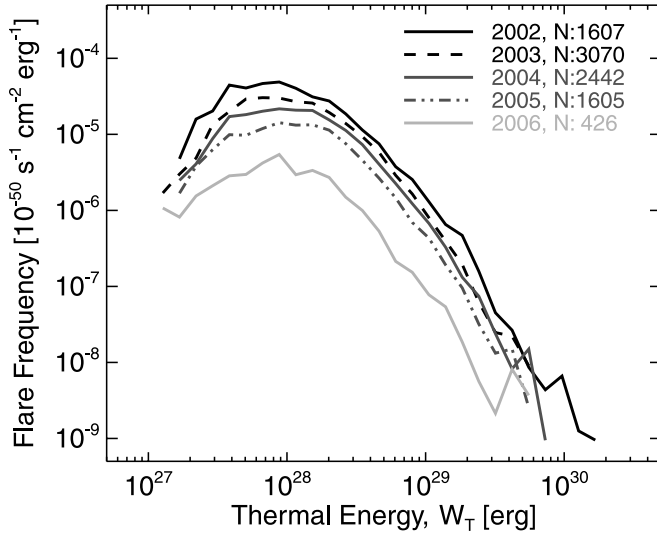


FIG. 19.—Frequency distribution of the microflare thermal energy, each line indicating a different year. The number quoted next to the year is the number of events from each year used in the distribution.

physical processes. Second, the distributions cover different phases of the solar cycle. The previous studies show a snapshot of the energy distribution of different small energy release features in the solar corona, whereas the *RHESSI* microflare energy distribution represents 5 years of observations of the declining phase of the solar cycle. The difficulty here lies in determining whether these snapshot surveys demonstrate typical or unusual behavior. Using the *RHESSI* thermal energies, we can investigate how the energy distribution changes with time by plotting the distributions for each year separately, as shown in Figure 19. These distributions have similar shapes except that the normalization decreases by over an order of magnitude between 2002 and 2006. So the non-*RHESSI* distributions in Figure 18 could be shifted vertically by a considerable amount if they were found during a different part of the solar cycle. This invariance in the shape of the distribution during the solar cycle has been found previously in both soft (Feldman et al. 1997; Veronig et al. 2002) and hard (Crosby et al. 1993; Lu et al. 1993) X-rays and also illustrates that the selection effects on the *RHESSI* data do not vary with time.

4.2. Nonthermal Power Frequency Distributions

To calculate the power in accelerated electrons from the information about the power law in the photon spectrum, we use

γ and I_0 (the power-law index and normalization) found in § 3 in equation (4). However, there is ambiguity as to the low-energy cutoff E_C because the observed photon spectrum depends only weakly on it. In addition, the *RHESSI* microflare spectrum covers both the thermal and nonthermal energy ranges, so there is inherent ambiguity. Previous studies used their X-ray threshold for E_C resulting in large uncertainties in the energy estimates (Crosby et al. 1993; Lin et al. 2001). As *RHESSI* makes spectral measurements down to the thermal component, we can provide a better estimate of the nonthermal energy content. In Paper I a fixed E_C was used to provide a rough estimate of the nonthermal power at peak time (Paper I). The full spectrum fitting in § 3 provides a better estimate of the parameters required to calculate the nonthermal power via equation (4). However, despite this improvement, we only have an estimate of where the photon spectrum begins to flatten (ϵ_B) and not the actual cutoff in the electron distribution E_C .

To obtain an estimate of E_C we have therefore investigated how the fitted broken power-law model relates to the expected photon spectrum from the electron distribution using the numerical integration code of Holman (2003). An example of this is shown in the left panel of Figure 20, where the photon spectrum for an electron distribution with $\delta = 8$ and E_C was calculated and then fitted with a broken power law in the same manner as that used for the microflare spectrum. This broken power law has $\gamma = 7.03$, expected as $\delta \equiv \gamma + 1$ (Brown 1971), above a break of $\epsilon_B = 6.06$ keV. Repeating this process for various values of the electron distribution parameters δ and E_C shows how the resulting fitted ϵ_B scales with these parameters. This is shown in the middle panel of Figure 20, where ϵ_B is given against E_C for three different values of δ . For a single value of δ , E_C approximately scales linearly with ϵ_B , and this scaling steepens with increasing δ . So we can approximate this relationship to first order by linearly fitting the relationship between ϵ_B and E_C for various δ and then linearly fitting how the parameters of the first fit vary with δ . This empirical relationship between the observed parameters of the photon power-law γ , ϵ_B and the low-energy cutoff of the electron distribution E_C can be found:

$$E_C \approx 0.15\gamma + (1.86 - 0.04\gamma)\epsilon_B - 3.39. \quad (6)$$

Using equation (6) the values of γ and ϵ_B for the 4236 microflares with trustworthy nonthermal spectral fits result in a histogram of E_C for these events, shown in the right panel of Figure 20. The low-energy cutoffs range from 9 to 16 keV with the median being about 12 keV, with generally $\epsilon_B \approx 0.75E_C$. The uncertainty in E_C can be seen in the average ratio of the error (found from the fit

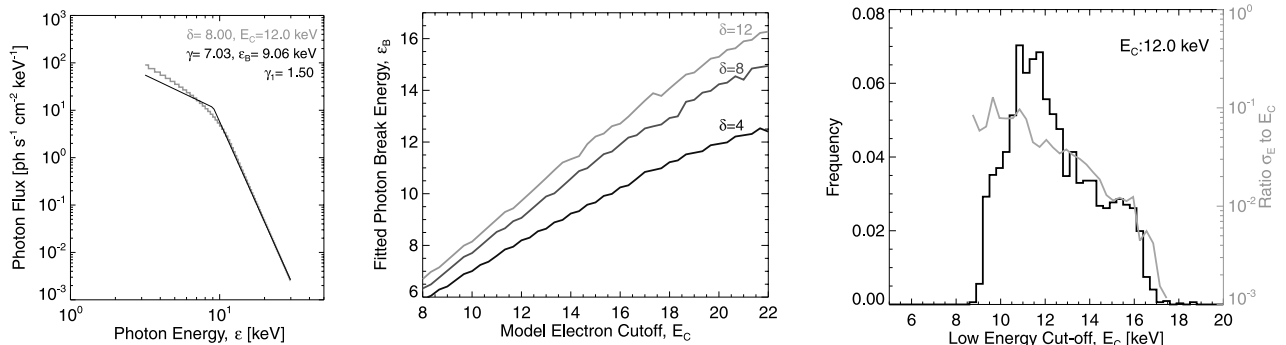


FIG. 20.—Left: Broken power-law fit to photon spectrum from a thick target model of a power-law electron distribution, using the code of Holman (2003). Middle: Fitted break energy ϵ_B of photon broken power-law against low-energy cutoff of electron distribution; the different lines indicate the different indices δ of the electron distributions. Right: Histogram of E_C for the 4236 microflares shown in Fig. 10. The gray line refers to the right-hand axis and shows the average ratio of the error to E_C as a function of E_C .

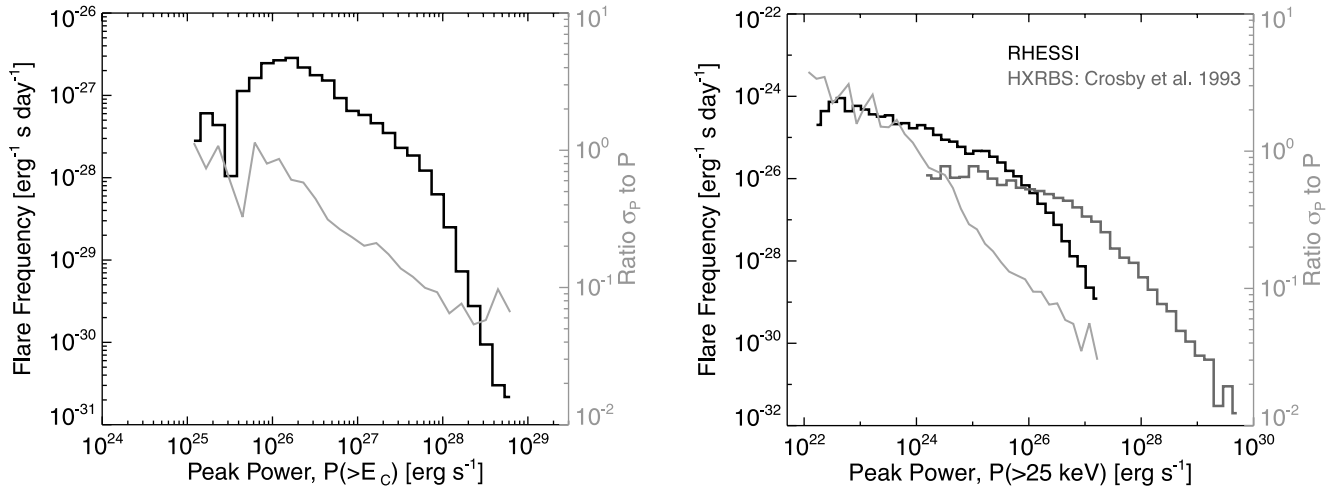


FIG. 21.—Frequency distribution of the nonthermal power of 4236 *RHESSI* microflares for $P(>E_C)$ (left) and $P(>25 \text{ keV})$, in comparison to the distribution found by Crosby et al. (1993) for large flares (right). The gray lines refers to the right-hand axes and show the average ratio of the error in the power to the power, as a function of the power. [See the electronic edition of the Journal for a color version of this figure.]

errors in γ and ϵ_B) to E_C , also shown in the right panel of Figure 20. For $E_C < 12 \text{ keV}$, where the majority of the events lie, the uncertainty is about 10% and drops to about 1% for the few events with larger E_C .

These values of E_C can then be used in equation (4) to calculate the power in nonthermal electrons above E_C , $P(\geq E_C)$, the frequency distribution of which is shown in the left panel of Figure 21. Here the power ranges over 10^{25} – $10^{28} \text{ erg s}^{-1}$, with the median being about $10^{26} \text{ erg s}^{-1}$. Also shown is the ratio of the error to the power, as a function of the power. The few microflares that show a power of $\sim 10^{28} \text{ erg s}^{-1}$ have the smallest errors with uncertainties about 10%. These powers seem relatively high for small flares, as the *RHESSI* power estimates in large flares are 10^{27} – $10^{30} \text{ erg s}^{-1}$ (Holman 2003; Emslie et al. 2004; Saint-Hilaire & Benz 2005; Sui et al. 2005, 2007), although it should be noted that the nonthermal emission in microflares lasts for $\approx 10 \text{ s}$, whereas it can last for tens of minutes in large flares. The total nonthermal energy content in large flares is many orders of magnitude larger than in microflares. The majority of the microflares shown in Figure 21 show nonthermal powers considerably smaller than this level, although with increasing uncertainty. The median power of $10^{26} \text{ erg s}^{-1}$ has about a 50% error, and the smallest events at $10^{25} \text{ erg s}^{-1}$ have almost 100% error. It is this large uncertainty in the power that results in this distribution deviating from a power law. Although the selection effects and biases will affect this nonthermal distribution as seen in the thermal distribution, these effects are hidden by the large uncertainties. Since it deviates from a power law, it has not been fitted using this model.

To allow comparison to the power distribution in electrons above 25 keV $P(\geq 25)$ for 2878 large flares found over 1980–1982 using *SMM* HXRBS (Crosby et al. 1993), the same power is estimated in the *RHESSI* microflares, shown in the right panel of Figure 21. These powers using $E_C = 25 \text{ keV}$ for the *RHESSI* microflare ranges over 10^{22} – $10^{27} \text{ erg s}^{-1}$ with the median power being about $10^{24} \text{ erg s}^{-1}$. On this basis the *RHESSI* microflares cover events down to 2 orders of magnitude smaller than those in the *SMM* HXRBS study. Again, the error is smallest in the largest power estimates. This $P(\geq 25)$ *RHESSI* distribution deviates less from a power law than the $P(\geq E_C)$ distribution. This is because there is less uncertainty in the power estimate in the larger events as the fixed $E_C = 25 \text{ keV}$ has no associated error.

5. DISCUSSION AND CONCLUSIONS

We have analyzed 25,705 microflares, successfully recovering trustworthy spatial information about the thermal emission for 18,656 of them, as well as the thermal spectral fit in 9161 and the thermal and nonthermal fits in 4236. The median values and ranges of each of the microflare parameters are summarized in Table 1. As found in Paper I, the microflares occur only in active regions, and this immediately suggests that these events are ill-suited to heat the overall corona. It also helps to show that the X-ray emission outside active regions, especially during periods of quiet Sun, is considerably smaller than the smallest active-region flares observed with *RHESSI*. This is confirmed by the *RHESSI* quiet-Sun study (Hannah et al. 2007), which found a limit on the flux over 2 orders of magnitude smaller than that of the smallest microflares found here.

Forward-fitting the visibilities of *RHESSI* data is a fast and efficient way to recover the spatial information (Hurford et al. 2005). We find that the thermal emission (4–8 keV) of the microflares shows predominantly looplike structures that have a median width of $11''$ and $32''$ length. Those events where no

TABLE 1
MEDIAN AND RANGE OF *RHESSI* MICROFLARE PARAMETERS

Microflare Parameter	Median Value	Range (5%–95%)
Duration D^a	5.4 minutes	2.2–15 minutes
Temperature T	12.6 MK	10.7–15.5 MK
Emission measure EM	$3 \times 10^{46} \text{ cm}^{-3}$	4×10^{45} to $2 \times 10^{47} \text{ cm}^{-3}$
Thermal loop width w	8 Mm ($11''$)	3–20 Mm ($4''$ – $28''$)
Thermal loop length l	23 Mm ($32''$)	7–77 Mm ($10''$ – $107''$)
Thermal loop volume V	$1 \times 10^{27} \text{ cm}^3$	5×10^{25} to $2 \times 10^{28} \text{ cm}^3$
Density n_e	$6 \times 10^9 \text{ cm}^{-3}$	8×10^8 to $3 \times 10^{10} \text{ cm}^{-3}$
Power-law index γ	7	4–10
Break energy ϵ_B	9 keV	7–12 keV
Low-energy cutoff E_C	12 keV	9–16 keV
Thermal energy W_T^b	10^{28} erg	10^{26} – 10^{30} erg
Nonthermal power $P_N(\geq E_C)^b$	$10^{26} \text{ erg s}^{-1}$	10^{25} – $10^{28} \text{ erg s}^{-1}$
Nonthermal power $P_N(\geq 25)^b$	$10^{24} \text{ erg s}^{-1}$	10^{22} – $10^{27} \text{ erg s}^{-1}$

^a Values from Paper I; 1 minute lower limit due to selection effects.

^b All parameters are estimated from analysis using 16 s around the time of peak emission in 6–12 keV, so resulting energy estimates are for those times.

spatial information was recoverable were predominantly those with the fewest counts, although some larger events produce poor spatial information as there were other instrumental issues. These spatial scales do not correlate with the magnitude of the microflare, the 4–8 keV flux from the loop nor the *GOES* class, and so small flares are not necessarily spatially small. This may be due to the prevalence of a typical loop scale size associated with active regions, and it is independent of the amount of energy the flare has deposited into heating the material that evaporates to fill these loops. In the largest flares this energy might be deposited over a larger area, evaporating material into more loops, hence, the larger structures and arcades that are observed. The widths of these loops may not be as well resolved as the lengths, with the observed single *RHESSI* loop possibly being several narrow and long loops beside each other, as observed in microflare with *RHESSI* and *Hinode* XRT (Hannah et al. 2008). The volume of these loops can be estimated, the median value being 1×10^{27} cm³. This volume estimate assumes a cylindrical geometry and filling factor of unity, meaning that our volumes, and hence thermal energies, are upper limits, as this filling factor can be < 1 (Cargill & Klimchuk 1997; Takahashi & Watanabe 2000).

We find that microflares are hot, with a median temperature of 13 MK. In these microflares the median emission measure is 3×10^{46} cm⁻³, which combined with the volume allows a density of 6×10^9 cm⁻³ to be calculated. As the volume may be an overestimate, this means that the density might be underestimated. The presence of the spectral feature due to the Fe K-shell transitions proves that there really is hot plasma present with $T > 8$ MK (Phillips 2004). Correlations between the temperature and other parameters are difficult to extract from our sample due to the temperature selection effect, resulting in only a relative narrow range of temperatures being sampled. Studying larger flares would aid by extending the range of flare temperatures, but this would be complicated by systematic effects related to *RHESSI*'s attenuating shutters. An alternative would be to investigate this selection effect by comparing model spectra for known temperatures and emission measures with those found by fitting this spectrum once noise and the instrumental response have been included. This has already been attempted for the *TRACE* nanoflares study (Aschwanden & Parnell 2002), and it revealed a difference between the observed parameters and the “intrinsic” ones. Another way of investigating the instrumental response and biases is in comparison to results from other instruments. We have found that the *GOES* emission measures are typically a factor of 2 larger than those found with *RHESSI*. This may be due to the underlying DEM in microflares scaling similarly but might also be due to the instrument's relative sensitivity. This could be further studied by forward-fit modeling of the instrumental responses to recover the underlying DEM in each event (Aschwanden & Alexander 2001), instead of assuming a constant emission measure.

The thermal energies for the peak time in these microflares were found to range from 10^{26} to 10^{30} erg with the median energy being 10^{28} erg. The thermal energy distribution deviates from a power law at low and high energies, but this can be explained by selection effects and does not suggest that the underlying true distribution is not power law. The smallest events are missing as they do not have enough counts to be found either above solar or instrumental background, successfully imaged or spectrally analyzed. The larger events are missing from the distribution due to *RHESSI*'s attenuating shutters, so either they are excluded from our selection or have poor detector live time. Although it is possible to extend this energy distribution to higher energies by analyzing all large flares observed with *RHESSI*, there will still be a strong instrumental effect at the shutter transition due to

detector live-time effects. The statistical errors in the fitted parameters will affect the thermal energy estimates, but these have a relatively small effect compared to the selection effects. The greatest uncertainty is the systematic error that arises from the filling factor used to estimate the thermal volume: taking an extreme filling factor of $f \approx 10^{-4}$ (Cargill & Klimchuk 1997) would have the effect of reducing the energies by a factor of 100. Therefore, the thermal energies quoted here about the time of peak emission in 6–12 keV are upper limits. The comparison of the *RHESSI* thermal distribution to other thermal distributions of other transient coronal energy releases is difficult as these events are from a limited sample of events over a very short time period.

With *RHESSI* we are able to investigate the flattening of the nonthermal photon spectrum and can empirically estimate the low-energy cutoff E_C in the electron distribution from the observed photon spectrum. However, we are only able to successfully fit the nonthermal spectral component, in addition to the thermal component, in 4236 events. The difficulty in successfully finding and fitting this nonthermal emission arises from the steep spectra that start close to the thermal spectral features about 7 keV. So although the nonthermal component was only successfully fitted in a minority of events, it does not mean that there is a lack of accelerated electrons in the others. It does mean, however, that the relatively large uncertainties in the nonthermal parameters will result in large uncertainties in E_C and the nonthermal power estimates. These large uncertainties and the biases introduced by rejecting many events due to poor spectral fits can be easily seen in the histograms of the nonthermal parameters γ and ϵ_B . We find that the microflares typically have nonthermal emission represented by a broken power law with index $\gamma = 7$, break at 9 keV. We can estimate $E_C = 12$ keV for breaks in the photon spectrum above 7 keV.

These nonthermal parameters were used to calculate the power in accelerated electrons above E_C , which range over 10^{25} – 10^{28} erg s⁻¹ with a median value of 10^{26} erg s⁻¹. This distribution again deviates from a power law at low and high energies due to the uncertainties in the power estimates and the rejected events due to poor spectral fits rather than the selection effects present in the thermal distribution. The uncertainties in the few events with the largest nonthermal component are only $\sim 10\%$, so this cannot explain the fact that in some of these small flares the rate of energy release is comparable to larger flares, 10^{27} – 10^{30} erg s⁻¹ (Holman 2003; Emslie et al. 2004; Saint-Hilaire & Benz 2005; Sui et al. 2005, 2007). However, the nonthermal emission in microflares lasts for only \approx tens of seconds, whereas it can last for tens of minutes in large flares. The nonthermal energy content in large flares is thus many orders of magnitude larger than that in microflares. To make a direct comparison of these *RHESSI* microflare results to the peak nonthermal power distribution found for large flares by Crosby et al. (1993), the same instrumental $E_C = 25$ keV has to be used. On this basis the *RHESSI* microflare peak powers extend to 2 orders of magnitude smaller than the Crosby et al. (1993) study. The true nonthermal power in the Crosby et al. (1993) flares cannot be determined as the spectrum was not observed to sufficiently low energies, and so that study could have easily underestimated the nonthermal energy content. We conclude that the instantaneous nonthermal power in a microflare can be surprisingly large.

One further explanation for the unexpectedly large nonthermal power in the microflares might be that the physical model used is less suited for small flares than large. The energy in the accelerated electrons was found using the standard cold thick target model (Brown 1971). It has been suggested that for the lowest energy electrons the target is warm and not cold, and $5kT$

could be used as an approximate cutoff (Emslie 2003). Unfortunately for the microflares, this gives an even lower cutoff at around 4–5 keV, which results in an even larger nonthermal power estimate. Nevertheless, the idea of the nonthermal electron distribution smoothly transitioning into the thermal distribution seems physically more realistic than a sharp low-energy cutoff and may provide a clue to the physics of the energization of the electron distribution function. Another change to the model of the hard X-ray emission would be the inclusion of free-bound emissions (Brown & Mallik 2007), as our models currently only assume free-free continuum. Microflares might be the ideal type of flares to study this seldom-considered mechanism as the resulting additional spectral features would occur above 10 keV and would likely have been hidden by the thermal component in large flares. However, the temperatures required for such free-bound features to be present, ≥ 20 MK (Brown & Mallik 2007), are not typically observed in *RHESSI* microflares.

The analysis presented here is only performed at the time of peak 6–12 keV emission even though the most desirable results would investigate the full time range of each microflare, producing the total thermal and nonthermal energy estimates. But as this paper has shown, it is a considerable undertaking just ana-

lyzing this peak time period. The next steps in this microflare study would be to investigate the biases and instrumental effects using simulations and making improvements to the forward-fit model of the emission. Although *RHESSI* has for the first time allowed the thermal energy and nonthermal power distributions to be studied systematically in microflares, the uncertainty in the transition between thermal and nonthermal components highlights the instrumental effects and biases. We also have suggested the possibility that the standard hard X-ray model used is wrong. The model and instrumental effects could be studied by investigating the microflares not only with *RHESSI* but other instruments as well. It may, however, require an instrument with better energy resolution and lower instrumental background than *RHESSI* before we can unambiguously determine the energy component of microflares and decide whether there is an issue with the hard X-ray model used.

NASA supported this work under grant NAS5-98033 and NNG05GG16G. I. H. would like to thank L. Fletcher and C. Parnell, as well as the rest of the *RHESSI* team, for helpful discussions and M. Battaglia for providing flare data for comparison.

REFERENCES

- Aschwanden, M. J. 2007, *Adv. Space Res.*, 39, 1867
 Aschwanden, M. J., & Alexander, D. 2001, *Sol. Phys.*, 204, 91
 Aschwanden, M. J., & Parnell, C. E. 2002, *ApJ*, 572, 1048
 Aschwanden, M. J., et al. 2000, *ApJ*, 535, 1047
 Battaglia, M., Grigis, P. C., & Benz, A. O. 2005, *A&A*, 439, 737
 Benz, A. O., & Grigis, P. C. 2002, *Sol. Phys.*, 210, 431
 ———. 2003, *Adv. Space Res.*, 32, 1035
 Benz, A. O., & Krucker, S. 2002, *ApJ*, 568, 413
 Brown, J. C. 1971, *Sol. Phys.*, 18, 489
 Brown, J. C., & Mallik, P. C. V. 2007, *A&A*, submitted (arXiv: 0706.2823v1)
 Cargill, P. J., & Klimchuk, J. A. 1997, *ApJ*, 478, 799
 Christe, S., Hannah, I. G., Krucker, S., McTiernan, J., & Lin, R. P. 2008, *ApJ*, 677 (Paper I)
 Crosby, N., Aschwanden, M., & Dennis, B. 1993, *Sol. Phys.*, 143, 275
 Crosby, N., Vilmer, N., Lund, N., & Sunyaev, R. 1998, *A&A*, 334, 299
 Dere, K. P., Landi, E., Mason, H. E., Monsignori Fossi, B. C., & Young, P. R. 1997, *A&AS*, 125, 149
 Drake, J. F. 1971, *Sol. Phys.*, 16, 152
 Emslie, A. G. 2003, *ApJ*, 595, L119
 Emslie, A. G., et al. 2004, *J. Geophys. Res.*, 109, 10104
 Feldman, U., Doschek, G. A., & Behring, W. E. 1996a, *ApJ*, 461, 465
 Feldman, U., Doschek, G. A., Behring, W. E., & Phillips, K. J. H. 1996b, *ApJ*, 460, 1034
 Feldman, U., Doschek, G. A., & Klimchuk, J. A. 1997, *ApJ*, 474, 511
 Gallagher, P. T., Mathioudakis, M., Keenan, F. P., Phillips, K. J. H., & Tsinganos, K. 1999, *ApJ*, 524, L133
 Hannah, I. G., Hurford, G. J., Hudson, H. S., Lin, R. P., & van Bibber, K. 2007, *ApJ*, 659, L77
 Hannah, I. G., Krucker, S., Hudson, H. S., Christe, S., & Lin, R. P. 2008, *A&A*, in press (arXiv: 0712.0369)
 Holman, G. D. 2003, *ApJ*, 586, 606
 Hudson, H. S. 1991, *Sol. Phys.*, 133, 357
 Hurford, G. J., Schmahl, E. J., & Schwartz, R. A. 2005, *AGU Abstr. Spring*, A12
 Hurford, G. J., et al. 2002, *Sol. Phys.*, 210, 61
 Krucker, S., & Benz, A. O. 1998, *ApJ*, 501, L213
 Krucker, S., Benz, A. O., Bastian, T. S., & Acton, L. W. 1997, *ApJ*, 488, 499
 Krucker, S., Christe, S., Lin, R. P., Hurford, G. J., & Schwartz, R. A. 2002, *Sol. Phys.*, 210, 445
 Kundu, M. R., Schmahl, E. J., Grigis, P. C., Garaimov, V. I., & Shibasaki, K. 2006, *A&A*, 451, 691
 Kundu, M. R., Trotter, G., Garaimov, V. I., Grigis, P. C., & Schmahl, E. J. 2005, *Adv. Space Res.*, 35, 1778
 Landi, E., Del Zanna, G., Young, P. R., Dere, K. P., Mason, H. E., & Landini, M. 2006, *ApJS*, 162, 261
 Lee, T. T., Petrosian, V., & McTiernan, J. M. 1995, *ApJ*, 448, 915
 Lin, R. P. 1974, *Space Sci. Rev.*, 16, 189
 Lin, R. P., Feffer, P. T., & Schwartz, R. A. 2001, *ApJ*, 557, L125
 Lin, R. P., et al. 2002, *Sol. Phys.*, 210, 3
 Liu, C., Qiu, J., Gary, D. E., Krucker, S., & Wang, H. 2004, *ApJ*, 604, 442
 Lu, E. T., Hamilton, R. J., McTiernan, J. M., & Bromund, K. R. 1993, *ApJ*, 412, 841
 Parker, E. N. 1988, *ApJ*, 330, 474
 Parnell, C. E. 2004, in *Proc. SOHO 15 Workshop*, ed. R. W. Walsh et al. (Paris: ESA), 227
 Parnell, C. E., & Jupp, P. E. 2000, *ApJ*, 529, 554
 Phillips, K. J. H. 2004, *ApJ*, 605, 921
 Phillips, K. J. H., Bhatia, A. K., Mason, H. E., & Zarro, D. M. 1996, *ApJ*, 466, 549
 Qiu, J., Liu, C., Gary, D. E., Nita, G. M., & Wang, H. 2004, *ApJ*, 612, 530
 Saint-Hilaire, P., & Benz, A. O. 2005, *A&A*, 435, 743
 Schmahl, E. J., Pernak, R. L., Hurford, G. J., Lee, J., & Bong, S. 2007, *Sol. Phys.*, 240, 241
 Schwartz, R. 1996, *NASA STI/Recon. Tech. Rep. N*, 96, 71448
 Shimizu, T. 1995, *PASJ*, 47, 251
 Smith, D. M., et al. 2002, *Sol. Phys.*, 210, 33
 Stoiser, S., Veronig, A. M., Aurass, H., & Hanslmeier, A. 2008, *Sol. Phys.*, 246, 339
 Sui, L., Holman, G. D., & Dennis, B. R. 2005, *ApJ*, 626, 1102
 ———. 2007, *ApJ*, 670, 862
 Takahashi, M., & Watanabe, T. 2000, *Adv. Space Res.*, 25, 1833
 Tandberg-Hanssen, E., & Emslie, A. G. 1988, *The Physics of Solar Flares* (Cambridge: Cambridge Univ. Press)
 Veronig, A., Temmer, M., Hanslmeier, A., Otruba, W., & Messerotti, M. 2002, *A&A*, 382, 1070